ACS Photonics

pubs.acs.org/journal/apchd5

Letter

Resolving the Sequence of RNA Strands by Tip-Enhanced Raman Spectroscopy

Zhe He,[○] Weiwei Qiu,[○] Megan E. Kizer, Jizhou Wang, Wencong Chen, Alexei V. Sokolov, Xing Wang,* Jonathan Hu,* and Marlan O. Scully*

Cite This: *ACS Photonics* 2021, 8, 424−430

Read Online

ACCESS | Metrics & More | Article Recommendations | Supporting Information

ABSTRACT: RNA plays critical roles in guiding protein expression and catalyzing biological reactions. The gold standard RNA sequencing method requires converting RNA to complementary DNA (cDNA). This is followed by DNA amplification via polymerase chain reaction (PCR) and sequencing, making RNA sequencing indirect, complicated, and susceptible to sequence data bias. This paper demonstrates RNA imaging at the single-base level while illustrating a direct method to read RNA sequences by tip-enhanced Raman scattering (TERS) technique. To resolve nucleotides within an RNA strand, we adopted gap-mode TERS involving a gold tip and a gold substrate. After analyzing TERS measurements based on the reference sequence, we identified RNA sequences with 90% accuracy. This proof-of-principle RNA imaging method significantly advances a direct RNA sequencing technique without RNA labeling or reverse transcriptase RT-PCR amplification.

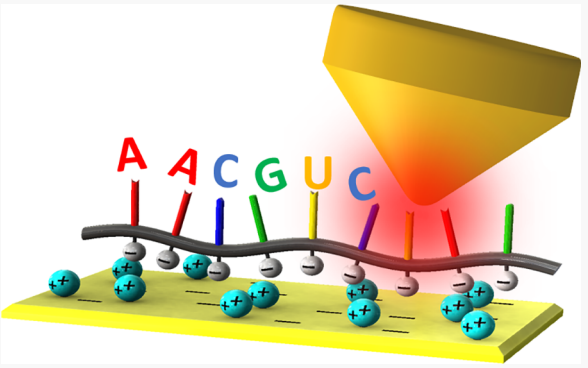

KEYWORDS: *Raman spectroscopy, nanotechnology, surface plasmon resonance, RNA*

RNA conveys rich information in disease diagnostics and fundamental understanding of disease states. For example, coronaviruses are enveloped RNA viruses.[1] The viral RNA genome extracted from bronchoalveolar-lavage fluid is currently used for COVID-19 diagnosis by RT-PCR based methods.[2] Circulating microRNAs serve as potential cancer biomarkers.[3] Furthermore, some RNAs are capable of regulating cancer-causing genes and some have been linked to various neurodegenerative diseases, including Alzheimer disease.[4] Thus, sequencing RNA transcripts and identifying modified RNA bases from patient samples can provide a detailed look at disease states, including different expression levels of transcripts and antisense transcription, and allusion to the structure of genes based on known correlations between RNA primary sequences and tertiary structures.[5] Furthermore, understanding the interplay between transcriptome sequences and protein information on expression levels and proteomes can elucidate many facets of human life and society, including the understanding of evolution and ecological systems as well as advances in agriculture, environmental science, and remediation (see examples in refs 6−22).

Sequencing technologies have underscored our ability to make progress in understanding such disease states. The gold standard technique relies on RNA isolation, reverse transcription, and amplification before sequencing. Not only is this process time-consuming, but the many steps also provide opportunities for introducing errors into the final sequencing result. Microarray technologies have expedited the process. The current next-generation sequencing (NGS) technologies[23] allow high-throughput RNA-seq through complementary DNA (cDNA) sequencing. Although NGS technologies have eliminated several challenges caused by microarray technologies, the cDNA-based transcriptome analysis approach displays several limitations that restrict us from fully understanding the nature of transcriptomes and genome biology. More specifically, there are four major shortcomings: (1) the generation of spurious cDNA due to the DNA-dependent DNA polymerase activities;[24,25] (2) the generation of artificial cDNAs resulted from contaminating DNA or template switching[26−29] and primer-independent cDNA synthesis;[30,31] (3) the production of low quantities of cDNA due to the error-prone[32,33] and inefficacy of reverse transcriptase;[34] and (4) the bias introduced by PCR-based second-strand cDNA synthesis[35] due to reducing sequence complexity, distorting the relative cDNA abundances, skipping some RNA species, and losing chemical modifications on RNA bases. Considering these shortcomings, we are highly motivated to develop a new

Received: September 23, 2020
Published: December 10, 2020

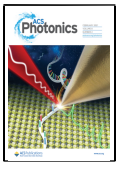

https://dx.doi.org/10.1021/acsphotonics.0c01486
ACS Photonics 2021, 8, 424−430

method that can directly map RNA transcripts without PCR amplification and detect antisense transcripts without involving artifacts of library preparation.[36] Further efforts will be required to reveal the presence and identity of RNA modifications and to generate continuous and long-range sequence reads that span splice junctions or repetitive elements.

Raman spectroscopy is commonly used in chemistry to provide a structural fingerprint to identify molecules.[37] However, the traditional approach fails to identify bonds at the single-molecule level. Raman spectroscopy is generally weak for biomolecules or usually overwhelmed by noise and background fluorescence, which is insufficient for identifying single-molecules in low-concentration samples. Raman has also been utilized as an imaging method, yet it falls short of resolving nanostructures because this diffraction-limited system is dependent on the wavelength of light used. Such resolution limitations can be overcome by employing tip-enhanced Raman scattering (TERS), a technique that combines surface-enhanced Raman scattering (SERS) and scanning probe microscopy to improve the Raman signal and enable a subnanometer spatial resolution.[38−41] TERS coupled with atomic force microscopy (AFM) manifests an estimated Raman signal enhancement in the range of 10^6 to 10^9 and, at the same time, maps multiple components of the sample.[42] The increase in spatial resolution and molecular information through the use of TERS has queried investigations into various biological samples including viruses,[43] bacteria,[44] and single-stranded DNA (ssDNA) molecules.[45−48]

In most previous reports on TERS, the nanoscale spatial resolution has been profoundly widely discussed.[49−52] In spite of the fact that oversized conventional tips were used, some experiments had proved that TERS could resolve nanostructures with a few nanometers or even subnanometer resolution.[53] Though the reason is still under debate, we believe that further analysis of the nanostructures themselves, and their obtained scans, can elucidate the role of nanofeatures dramatic resolving capability on the tip surface in achieving the remarkable resolution. As our tip was made via physical vapor deposition, the tip was expected to be covered by rough atomic-scale features deposition. Thence, the surface roughness played an essential role as a kind of "mini-tip" that did a further effort to confine the local light field to a nanometer scale.[52,53] It should be noted that, due to the atomic size of the "mini-tip", the total volume-integrated local field was a small fraction of the total power for the whole tip. Therefore, it was neglected in most research works targeting a bulky sample. As in single-molecule experiments, the local field near the tip and the "mini-tip" yields comparable enhancement of the Raman signals because the atomic structure may dominate the field intensity in the subnanometer area. The fine structures on our tips were assumed to be placed randomly, which might cause less spatial resolution and some random hotspots. In the future work, a well-protected fine structure may need to be fabricated on a tip to achieve a more reliable, repeatable TERS measurement.

In this report we present a direct TERS-based single-stranded RNA (ssRNA) imaging method that highlights three major developments: (1) a unique ssRNA deposition method to maximize nucleobase identification, (2) an effective "mini-tip" that provides the requisite resolution for single-molecule detection, and (3) a novel analytical method in which the nucleobase information is elucidated. RNA is much more conformationally flexible than DNA; as a result, RNA may coil and form complex inter- and intratertiary structures form before, during, or after surface deposition. By employing a unique deposition method, we were able to minimize strand coiling and maximize exposure of nucleobases to the AFM tip and obtain TERS mapping of RNA at a 0.5 nm resolution.[48] The tip employed in the current study was made via physical vapor deposition and, as a result, was expected to be covered by rough atomic-scale features. This surface roughness effectively afforded a "mini-tip," which can confine the light field to the nanometer scale and provide resolution appropriate for single-molecule imaging.[52,53] Important distinguishing characteristics of the different nucleobases are contained in minor features of the Raman spectrum. Thus, we employed a sophisticated analytical approach in this work to accurately decipher the requisite chemical information on the ssRNA nucleobases in a single-molecule Raman spectrum. We developed a method based on the Pearson correlation coefficient, where the correlation function is applied to multiple spectra with reference data[54] and evaluates their degree of similarity. Compared to fitting methods commonly used in Raman signal analysis, which require a high signal-to-noise ratio, the correlation coefficient can identify the spectral similarity in a way largely insensitive to noise. We were, therefore, able to determine ssRNA nucleobase sequences with an accuracy of 90%. Taken together, this report presents the utilization of TERS to map single molecules of ssRNA directly. Furthermore, the work presented herein lays the foundation for a future developments of single-molecule RNA sequencing methods.

RESULTS

Imaging. A HORIBA-AIST-NT system, which combines Raman scattering and atomic force microscopy, was utilized to obtain TERS information on RNA. In this report, a 4000 base CRISPR-associated protein 9 (Cas9) ssRNA was deposited on a gold substrate (50 nm thick) for TERS mapping. Figure 1a depicts the RNA deposition method, and Figure 1b shows a schematic of the TERS experimental setup. TERS probes were fabricated through metal deposition of 50 nm of Au on the Si tip (Appnano, Mountain View, CA). The 660 nm laser (400 μW) was focused on the tip using a 100X objective lens to stimulate localized surface plasmons. Backscattered Raman photons were collected through the same lens and filtered to remove residual laser light.

We first explored the RNA alignment by an AFM tip under tapping mode. Ideally, the AFM could identify the thickness feature of RNA based on the high precision in the vertical direction. However, due to the tip-broadening effect[55] in our experiment, AFM cannot resolve a nanostructure less than the tip size (50 nm). One RNA molecule is expected to be approximately 1.5 nm in width and 0.5 nm in height.[56] We chose a thin strand and identified its profile by AFM (Figure 2a). The corresponding measurements are shown in Figure 2b. The width is around 20 nm, and the height is around 1.2 nm, indicating that the strand is composed of two overlapping molecules. Even if the AFM is sensitive enough to measure a height of less than 1 nm, the limitation of spatial resolution makes single molecule sensing impossible. We, therefore, determined that AFM was not sensitive enough to study single-strand RNA and pursued TERS as a more viable option.

TERS was conducted simultaneously with AFM scanning using a step-based contact mode approach. At each step, the

https://dx.doi.org/10.1021/acsphotonics.0c01486
ACS Photonics 2021, 8, 424−430

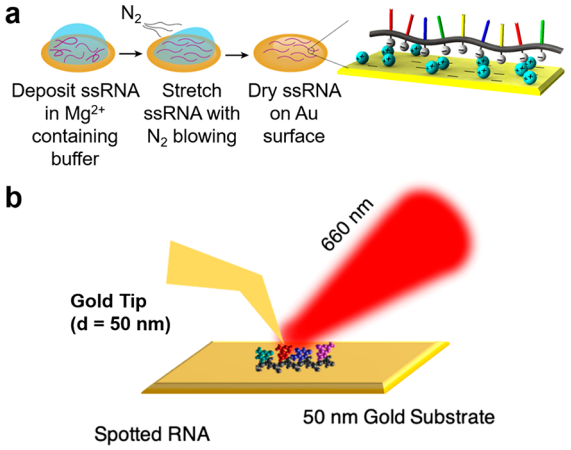

Figure 1. (a) RNA deposition method. We used compressed nitrogen to align the RNA on the gold surface and evade RNA coiling during deposition. Furthermore, Mg^{2+} cations were added in the RNA buffer solution (pH 7.5) to facilitate the adhesion of negatively charged RNA phosphate backbone to the gold surface. This will help to expose nucleobases to the tip for the downstream sensing and sequencing. Each "+" sign indicates an Mg^{2+} ion, and "−" sign indicates the negative charge carried by the RNA phosphate backbone or the gold surface. (b) Schematic of tip-enhanced Raman scattering. The diameter of the gold tip is 50 nm. An objective (100×, NA 0.7) focuses the 660 nm incidence light on the tip at 45°. The same objective collects TERS signals.

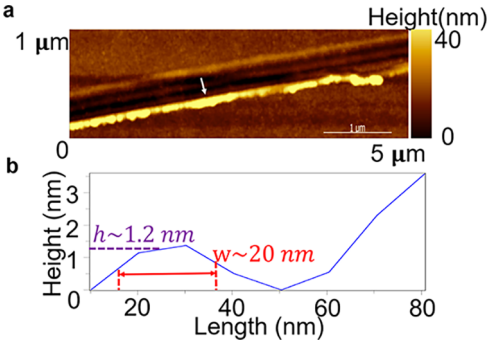

Figure 2. AFM image of RNA. (a) A few long RNA strands. As the approximate width is given by 20 nm, we assume that some RNA molecules were bundled. The white arrow shows the cross line of a single molecule. (b) The thickness profile along the white arrow in (a). The height profile shows a strand of 1.2 nm thickness and a 20 nm width.

tip was in contact with the sample for 4 s to produce a reasonably high signal-to-noise ratio. Since long-time contact at one spot can possibly cause tip drift, a longer acquisition time should be avoided. In this experiment, a 4 s acquisition provided an optimal balance between acceptable signal intensity and minimal tip drift. Figure 3a shows the TERS signal intensity of 1370 cm^{-1} along the RNA strand during a 0.5 nm contact step.

The imaging intensity is the integral counts of spectra between 1353 and 1387 cm^{-1}. This peak appeared stronger than others because it is composed of multiple bands from all nucleobases, including adenine, C2−H (1371 cm^{-1}), N9−H (1374 cm^{-1}), str C8−N9 (1372 cm^{-1}), C4−N9 (1372 cm^{-1}); guanine, in ring str C−N (1385 cm^{-1}), C−C (1376 cm^{-1}), rock NH2 (1382 cm^{-1}), bend N1/9-H (1388 cm^{-1}); uracil, in ben N3−H (1374 cm^{-1}), C5−H (1372 cm^{-1}), C6−H (1372 cm^{-1}); cytosine, in ben N1−H (1387 cm^{-1}), C5−H (1373 cm^{-1}), C6−H (1373 cm^{-1}).[54] Therefore, the spectral region utilized in Figure 3a can identify RNA but not distinguish the identity of individual nucleobases.

Determining RNA Sequences. To identify individual nucleobases, a more sophisticated analytical approach must be employed. This involves first the determination of reference peaks for each nucleobase, followed by the correlation of sample spectra to reference spectra to extract sequence information. Table S1 shows the assignment of each nucleobase characteristic reference peaks along with their normalized amplitudes. Raman peaks at 1325−1333 (A1), 1483−1491 (A2), 1303−1311 (C1), 1423−1431 (C2), 1457−1465 (G1), 1566−1574 (G2), 1046−1054 (U1), 1275−1283 (U2) are labeled to distinguish the four RNA bases: adenine (A), cytosine (C), guanine (G), and uracil (U).[54] At ambient conditions, the TERS technique may heat the sample and result in thermally induced peak shifts. Therefore, the center frequencies of Raman peaks are allowed in a range of frequencies.[57] The reference spectra take this error into consideration; the resulting allowable frequency ranges for the reference peaks are indicated by the colored areas in Figure S1. We employ dual-peak Gaussian functions to build the reference spectra intensities, P_{ref}, for A, C, G, and U, as described in eq 1:

$$P_{ref} = A_1 e^{-(x-x_1)^2/2\sigma_1^2} + A_2 e^{-(x-x_2)^2/2\sigma_2^2} \quad (1)$$

A_1 and A_2 represent the respective amplitudes of the reference peaks normalized to the maximum of A_1 and A_2, as only peak ratios are later used to calculate the correlation coefficient. The peak ratios of the two peaks assigned to one nucleobase were obtained from ref 54. The parameters x_1 andx_2 are the reference peak centers, and σ_1 and σ_2 represent the bandwidths. The full-width-half-maximum (fwhm) is 8 cm^{-1} for all peaks.

Since the characteristic peaks are unique for each nucleobase, they present at relatively low intensity in a measured sample spectrum and, as a result, require stringent analytical processing to determine nucleobase identity successfully. From a measured sample spectrum, we first searched for each peak at the frequencies defined in Table S1 and Figure S1. We then applied a discrete Pearson correlation function using the reference spectrum. The correlation evaluation is as follows:

$$\mathrm{Corr}(P, P_{ref}) = \frac{\sum (P - \bar{P})(P_{ref} - \bar{P}_{ref})}{\sqrt{\sum (P - \bar{P})^2}\sqrt{\sum (P_{ref} - \bar{P}_{ref})^2}} \quad (2)$$

where P and P_{ref} are the intensities of the sample and reference spectra. The values $\bar{P}$ and $\bar{P}_{ref}$ are the average values of P and P_{ref}. The peak with maximum $\mathrm{Corr}(P, P_{ref})$ was retained for nucleobase identification. This guarantees that minute peak features in the prospect area could be discovered. Figures S3 and S4 demonstrate this approach with the spectra of different nucleobases in different samples. Finally, we calculated the probabilities

$$P_i = \frac{\mathrm{Corr}_i}{\sum_j \mathrm{Corr}_j} \quad (3)$$

of the four nucleobases by normalizing the correlation coefficient of all four P_{ref}. The measured nucleobase identity was determined by selecting that with the maximum

https://dx.doi.org/10.1021/acsphotonics.0c01486
ACS Photonics 2021, 8, 424−430

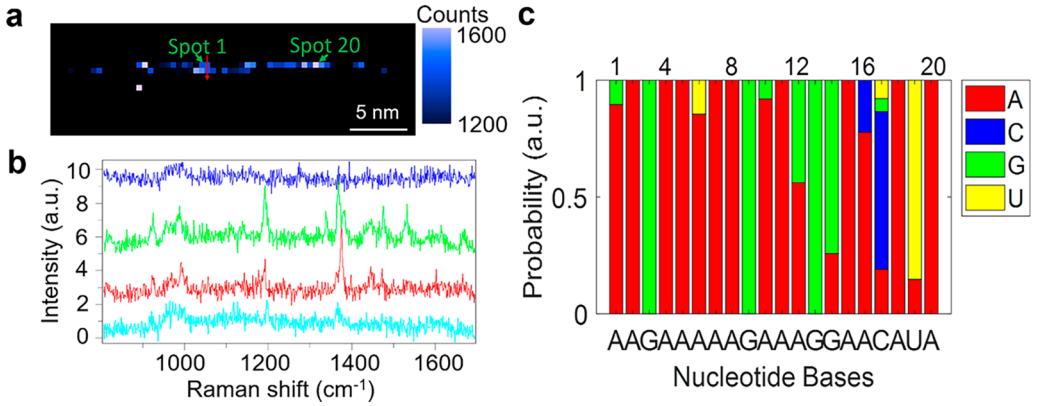

Figure 3. TERS signals of RNA. (a) Image of the plotting of the integral intensity of the peak 1370 cm^{-1}. The scanning step size is 0.5 nm. (b) Four spectra along the red arrow in (a). The contrast between the off-strand signals (cyan, blue) and the on-strand signals (red, green) indicates the spatial resolution less than 1 nm. (c) Measured sequence along the strand. A total of 20 nucleotides were measured in total. Spots 1 and 20 are labeled in (a). The most probable bases are labeled at the bottom. Compared to the real RNA sequence AAGAAAAAGAAAGGAUCCUA, two errors were found at spots 16 (U → A) and 18 (C → A).

probability (Figure 3c). Using the above procedure, we determined the sequence of a selected fragment of RNA to be AAGAAAAAGAAAGGAUCCUA, showing a sequence accuracy of 90%.

DISCUSSION

This report presents the use of a gap-mode TERS-AFM system to image and subsequently sequence ssRNA. Figure 3c illustrates the nucleobase sequence determination of a segment of ssRNA through our dual-Gaussian/Pearson coefficient correlation method. The most probable bases are labeled below the bars, and the resulting sequence was 90% accurate. There remain a few significant points which, upon further work with this method, will aid in propelling the TERS technique from an ssRNA imaging technique to an ssRNA sequencing technique.

Furthermore, since the nucleobases are not significantly spatially separated from each other in the ssRNA, they are likely close enough to affect adjacent signals. Though the "mini-tip" can resolve a single nucleobase, the local field of the whole tip could cover multiple bases. As a result, the interference from the surrounding nucleobases increases the error of sequencing. The curved alignment of RNA exacerbates this problem as nucleotides could be overlapped in a coiled area. Compared with the reference RNA sequences, we found that spots 16 and 18 were misread due to the strong neighboring guanine and adenine signals, which resulted in the 90% accuracy of our measurement. This is exemplified in Figure S2, where the Raman spectra of each step and, therefore, each base are shown.

Moreover, six repeated measurements with different tips and different samples are demonstrated in Table S2 and Figures S4 and S5, which all agree with the declared accuracy. Yet the curvature of the RNA strand still does not exactly align with the scanning direction, making accurate longer reads more challenging. A pertinent solution is to consider adjacent spots above or below the targeted nucleobase; one nucleotide may lead to signals in multiple pixels. The actual spectrum for each base was determined according to the base peaks with the highest probabilities. For example, the red and green curves in Figure 3b represent the Raman spectra of adjacent pixels, and they carry almost similar peaks. We evaluated both pixels to select the most correlated nucleotide. Repeating the calculations, sequences of a curved RNA fragment could be estimated. More complex, long, or coiled RNA species would require a more intricate algorithm or machine learning to extract an accurate sequence.

With TERS, single-molecule RNA imaging is challenging due to weak signals, nanoscale dimensions, and instability, especially in the ambient conditions. As the Raman cross-section of a single nucleobase is even smaller than the RNA backbone, weak signals were expected in these experiments. Because long RNA molecules are naturally coiled and bundled, it is even more difficult to explore their chemical components at the single-molecule level. In Figure 3, we present a high spatial resolution of TERS that overcomes the above technical challenges. In addition, in Figure S6, we display the image of a 400-base RNA strand that includes the segment shown in Figure 3. The strand occupies at least three lines and exposes no breakpoint. This indicates that TERS scanning of RNA did not fall short of maintaining the molecule.

Yet determining the complete 400-base sequence by TERS remained elusive as the properties of the longer RNA strand mentioned before diminishes spatial resolution and obfuscates spectral information. In our previous work,[48] a DNA strand was realigned along the scanning direction by the tip, which suggested that the tip could move molecules and straighten the RNA strand for optimal sequencing. However, the corresponding tip−RNA interaction is insufficient to realign the strand along the scanning direction and maintain the Raman signal. Rather, scanning RNA sequences required a relatively soft scan along the strand. Therefore, we set a softer compression force under contact mode and worked with a long RNA strand. The TERS scanning was performed with the contact mode known as the "Spec-top mode" (HORIBA-AIST), where the tip contacted the sample at each spot for 4 s before it was lifted to the next spot. A 30 nN force was applied to the sample, which may cause tip contamination and affect the RNA orientation. Under this mode, the tip can read and realign the molecule much more easily when the RNA strand contains one molecule and is relatively short. An example of this is shown in Figure S6, where a long single strand was not perfectly aligned along the scanning direction. Moreover, an even thicker strand is displayed in Figure S7, where the tip could not align it. As such, TERS has managed to provide stable imaging but only resolve nucleotide sequences of a shorter RNA fragment.

https://dx.doi.org/10.1021/acsphotonics.0c01486
ACS Photonics 2021, 8, 424−430

Additionally, tip contamination could be toxic to the tip. The contaminated signals were observed in several trials because a dirty tip could be easily identified during TERS scanning. If the tip were contaminated, the "bright signals" would spread randomly in the image. As a result, the spatial resolution could be lost. Therefore, we conclude that the results in Figure 3 are contamination free. Though the contact mode could result in unpredicted failure, TERS scanning must be performed under this mode for two reasons: (1) we need to contact the molecule to ensure the gap-mode configuration, and (2) without contact, no signal could be observed. To improve the performance, the contact force, speed, time, and scanning rate were optimized (see Supporting Information for details).

The issues presented above, including the weak single-molecule Raman signal and thermal drift due to the scan at ambient conditions, the future effort of TERS nanoscale imaging would require larger enhancement factors, tips with fine structures, and a more effective data analysis method to read Raman spectra with a low signal-to-noise ratio. The results so far, though not 100% perfect, show an excellent example of exploring RNA by a sophisticated analysis of their tip-enhanced Raman scattering signals.

In conclusion, we present our proof-of-principle TERS-based direct ssRNA imaging method and employ unique spectral interpretation to sequence nucleobases. This work demonstrates high-resolution RNA imaging and identification of RNA nucleobases sequences at 4 s per base and 90% accuracy. Our approach can potentially benefit many facets of fundamental research, medical diagnostics, and society, including the emerging need for detecting and sequencing viral RNA genome at the single-molecule resolution to help curb the spread of highly contagious infectious diseases like COVID-19.[58−60] The best defense against a new outbreak is early detection, and single-molecule RNA TERS can assist in that pursuit.

■ ASSOCIATED CONTENT

Supporting Information

The Supporting Information is available free of charge at https://pubs.acs.org/doi/10.1021/acsphotonics.0c01486.

Sample preparation; AFM and TERS measurements; Data analysis; Peak assignment table of RNA; Spectral templates for A, C, G, U; Spectra of Figure 3a and A, C, G, U; Repeating results of spectroscopy and sequencing; Probability chart of sequencing; TERS image of a 400-base RNA; TERS image of an RNA without alignment (PDF)

■ AUTHOR INFORMATION

Corresponding Authors

Jonathan Hu − *Baylor University, Waco, Texas 76798, United States;* orcid.org/0000-0001-6426-3051; Email: jonathan_hu@baylor.edu

Xing Wang − *University of Illinois at Urbana−Champaign, Urbana, Illinois 61801, United States;* orcid.org/0000-0001-9930-3287; Email: xingw@illinois.edu

Marlan O. Scully − *The Institute for Quantum Science and Engineering, Texas A&M University, College Station, Texas 77840, United States; Baylor University, Waco, Texas 76798, United States;* Email: scully@tamu.edu

Authors

Zhe He − *The Institute for Quantum Science and Engineering, Texas A&M University, College Station, Texas 77840, United States;* orcid.org/0000-0002-8525-3650

Weiwei Qiu − *Zhejiang University of Science and Technology, Hangzhou, Zhejiang 310023, China; Baylor University, Waco, Texas 76798, United States*

Megan E. Kizer − *Massachusetts Institute of Technology, Cambridge, Massachusetts 02139, United States;* orcid.org/0000-0003-3549-8606

Jizhou Wang − *The Institute for Quantum Science and Engineering, Texas A&M University, College Station, Texas 77840, United States;* orcid.org/0000-0003-2605-7278

Wencong Chen − *Vanderbilt University Medical Center, Nashville, Tennessee 37203, United States*

Alexei V. Sokolov − *The Institute for Quantum Science and Engineering, Texas A&M University, College Station, Texas 77840, United States; Baylor University, Waco, Texas 76798, United States*

Complete contact information is available at: https://pubs.acs.org/10.1021/acsphotonics.0c01486

Author Contributions

○These authors contributed equally to this work. Z.H, J.H., X.W., A.V.S., and M.O.S. conceived the idea and designed the experiments/assays. Z.H. performed the tip-enhanced Raman scattering experiments. W.Q. and Z.H. developed the sequencing algorithm. M.E.K. and X.W. produced the RNA samples. W.Q., Z.H., J.W., and W.C. did the spectroscopy analysis. Z.H., W.Q., A.V.S., X.W., and J.H. discussed and wrote the manuscript. All authors contributed to the experiments and manuscript preparation.

Funding

This work was supported by the Office of Naval Research (Award No. N00014-20-1-2184), the Robert A. Welch Foundation (Award Nos. A1261 and A-1547), National Science Foundation (Grant No. PHY-2013771), the Air Force Office of Scientific Research (Award No. FA9550-20-1-0366 DEF), the National Science Foundation (Grant Nos. ECCS-1809622 and CHE-1609608), and by King Abdulaziz City for Science and Technology (KACST). Z.H. was supported by the Herman F. Heep and Minnie Belle Heep Texas A&M University Endowed Fund held/administered by the Texas A&M Foundation. W.Q. was supported by the China Scholarship Council (Grant No. 201808330655).

Notes

The authors declare no competing financial interest.

■ ACKNOWLEDGMENTS

We thank Zehua Han and Alexander Sinyukov for helpful discussions. All data needed to evaluate the conclusions in the paper are present in the paper and/or the Supporting Information. The data sets generated and/or analyzed during the current study are available from X.W. (xingw@illinois.edu), J.H. (jonathan_hu@baylor.edu), and M.O.S. (scully@tamu.edu).

■ REFERENCES

(1) Murray, R. S.; Brown, B.; Brain, D.; Cabirac, G. F. Detection of coronavirus RNA and antigen in multiple sclerosis brain. *Ann. Neurol.* **1992**, *31* (5), 525−533.

(2) Zhu, N.; Zhang, D.; Wang, W.; Li, X.; Yang, B.; Song, J.; Zhao, X.; Huang, B.; Shi, W.; Lu, R.; et al. A novel coronavirus from patients with pneumonia in China, 2019. *N. Engl. J. Med.* **2020**, *382* (8), 727−733.
(3) Wang, H.; Peng, R.; Wang, J.; Qin, Z.; Xue, L. Circulating microRNAs as potential cancer biomarkers: the advantage and disadvantage. *Clinical Epigenetics* **2018**, *10* (59), 1−10.
(4) Ardekani, A. M.; Naeini, M. M. The role of microRNAs in human diseases. *Avicenna journal of medical biotechnology* **2010**, *2* (4), 161.
(5) Wang, Z.; Gerstein, M.; Snyder, M. RNA-Seq: a revolutionary tool for transcriptomics. *Nat. Rev. Genet.* **2009**, *10* (1), 57−63.
(6) Aird, S. D.; da Silva, N. J.; Qiu, L.; Villar-Briones, A.; Saddi, V. A.; Pires de Campos Telles, M.; Grau, M. L.; Mikheyev, A. S. Coralsnake Venomics: Analyses of Venom Gland Transcriptomes and Proteomes of Six Brazilian Taxa. *Toxins (Basel)* **2017**, *9* (6), 187.
(7) Casimiro-Soriguer, C. S.; Munoz-Merida, A.; Perez-Pulido, A. J. Sma3s: A universal tool for easy functional annotation of proteomes and transcriptomes. *Proteomics* **2017**, *17* (12), 1700071.
(8) Evans, V. C.; Barker, G.; Heesom, K. J.; Fan, J.; Bessant, C.; Matthews, D. A. De novo derivation of proteomes from transcriptomes for transcript and protein identification. *Nat. Methods* **2012**, *9* (12), 1207−1211.
(9) Freiberg, J. A.; Le Breton, Y.; Tran, B. Q.; Scott, A. J.; Harro, J. M.; Ernst, R. K.; Goo, Y. A.; Mongodin, E. F.; Goodlett, D. R.; McIver, K. S.; Shirtliff, M. E. Global Analysis and Comparison of the Transcriptomes and Proteomes of Group A Streptococcus Biofilms. *mSystems* **2016**, *1* (6), na.
(10) Gao, C.; Wang, Y.; Shen, Y.; Yan, D.; He, X.; Dai, J.; Wu, Q. Oil accumulation mechanisms of the oleaginous microalga Chlorella protothecoides revealed through its genome, transcriptomes, and proteomes. *BMC Genomics* **2014**, *15*, 582.
(11) Gerling, I. C.; Solomon, S. S.; Bryer-Ash, M. Genomes, transcriptomes, and proteomes: molecular medicine and its impact on medical practice. *Arch. Intern. Med.* **2003**, *163* (2), 190−198.
(12) Liu, L. Y.; Charng, Y. C. Genome-wide survey of ds exonization to enrich transcriptomes and proteomes in plants. *Evol. Bioinf. Online* **2012**, *8*, 575−587.
(13) Lupberger, J.; Croonenborghs, T.; Roca Suarez, A. A.; Van Renne, N.; Juhling, F.; Oudot, M. A.; Virzi, A.; Bandiera, S.; Jamey, C.; Meszaros, G.; Brumaru, D.; Mukherji, A.; Durand, S. C.; Heydmann, L.; Verrier, E. R.; El Saghire, H.; Hamdane, N.; Bartenschlager, R.; Fereshetian, S.; Ramberger, E.; Sinha, R.; Nabian, M.; Everaert, C.; Jovanovic, M.; Mertins, P.; Carr, S. A.; Chayama, K.; Dali-Youcef, N.; Ricci, R.; Bardeesy, N. M.; Fujiwara, N.; Gevaert, O.; Zeisel, M. B.; Hoshida, Y.; Pochet, N.; Baumert, T. F. Combined Analysis of Metabolomes, Proteomes, and Transcriptomes of Hepatitis C Virus-Infected Cells and Liver to Identify Pathways Associated With Disease Development. *Gastroenterology* **2019**, *157* (2), 537−551.
(14) Morsczeck, C.; Schmalz, G. Transcriptomes and proteomes of dental follicle cells. *J. Dent. Res.* **2010**, *89* (5), 445−456.
(15) Neerukonda, S. N.; Tavlarides-Hontz, P.; McCarthy, F.; Pendarvis, K.; Parcells, M. S. Comparison of the Transcriptomes and Proteomes of Serum Exosomes from Marek's Disease Virus-Vaccinated and Protected and Lymphoma-Bearing Chickens. *Genes* **2019**, *10* (2), 116.
(16) Obermeier, B.; Mentele, R.; Malotka, J.; Kellermann, J.; Kumpfel, T.; Wekerle, H.; Lottspeich, F.; Hohlfeld, R.; Dornmair, K. Matching of oligoclonal immunoglobulin transcriptomes and proteomes of cerebrospinal fluid in multiple sclerosis. *Nat. Med.* **2008**, *14* (6), 688−693.
(17) Rohousova, I.; Subrahmanyam, S.; Volfova, V.; Mu, J.; Volf, P.; Valenzuela, J. G.; Jochim, R. C. Salivary gland transcriptomes and proteomes of Phlebotomus tobbi and Phlebotomus sergenti, vectors of leishmaniasis. *PLoS Neglected Trop. Dis.* **2012**, *6* (5), No. e1660.
(18) Wagner, W.; Feldmann, R. E., Jr.; Seckinger, A.; Maurer, M. H.; Wein, F.; Blake, J.; Krause, U.; Kalenka, A.; Burgers, H. F.; Saffrich, R.; Wuchter, P.; Kuschinsky, W.; Ho, A. D. The heterogeneity of human mesenchymal stem cell preparations–evidence from simultaneous analysis of proteomes and transcriptomes. *Exp. Hematol.* **2006**, *34* (4), 536−548.
(19) Wan, H.; Cui, Y.; Ding, Y.; Mei, J.; Dong, H.; Zhang, W.; Wu, S.; Liang, Y.; Zhang, C.; Li, J.; Xiong, Q.; Qian, W. Time-Series Analyses of Transcriptomes and Proteomes Reveal Molecular Networks Underlying Oil Accumulation in Canola. *Front. Plant Sci.* **2017**, *7*, na.
(20) Wastling, J. M.; Xia, D.; Sohal, A.; Chaussepied, M.; Pain, A.; Langsley, G. Proteomes and transcriptomes of the Apicomplexa–where's the message? *Int. J. Parasitol.* **2009**, *39* (2), 135−143.
(21) Whaite, A. D.; Wang, T.; Macdonald, J.; Cummins, S. F. Major ampullate silk gland transcriptomes and fibre proteomes of the golden orb-weavers, Nephila plumipes and Nephila pilipes (Araneae: Nephilidae). *PLoS One* **2018**, *13* (10), No. e0204243.
(22) Zhang, H.; Egger, R. L.; Kelliher, T.; Morrow, D.; Fernandes, J.; Nan, G. L.; Walbot, V. Transcriptomes and proteomes define gene expression progression in pre-meiotic maize anthers. *G3: Genes, Genomes, Genet.* **2014**, *4* (6), 993−1010.
(23) Metzker, M. L. Sequencing technologies - the next generation. *Nat. Rev. Genet.* **2010**, *11* (1), 31−46.
(24) Gubler, U. Second-strand cDNA synthesis: classical method. *Methods Enzymol.* **1987**, *152*, 325−329.
(25) Spiegelman, S.; Burny, A.; Das, M. R.; Keydar, J.; Schlom, J.; Travnicek, M.; Watson, K. DNA-Directed DNA Polymerase Activity in Oncogenic Rna Viruses. *Nature* **1970**, *227* (5262), 1029−1031.
(26) Cocquet, J.; Chong, A.; Zhang, G. L.; Veitia, R. A. Reverse transcriptase template switching and false alternative transcripts. *Genomics* **2006**, *88* (1), 127−131.
(27) Mader, R. M.; Schmidt, W. M.; Sedivy, R.; Rizovski, B.; Braun, J.; Kalipciyan, M.; Exner, M.; Steger, G. G.; Mueller, M. W. Reverse transcriptase template switching during reverse transcriptase-polymerase chain reaction: Artificial generation of deletions in ribonucleotide reductase mRNA. *J. Lab. Clin. Med.* **2001**, *137* (6), 422−428.
(28) Roy, S. W.; Irimia, M. When good transcripts go bad: artifactual RT-PCR 'splicing' and genome analysis. *BioEssays* **2008**, *30* (6), 601−605.
(29) Roy, S. W.; Irimia, M. Intron mis-splicing: no alternative? *Genome Biology* **2008**, *9* (2), 208.
(30) Haddad, F.; Qin, A. X.; Bodell, P. W.; Zhang, L. Y.; Guo, H.; Giger, J. M.; Baldwin, K. M. Regulation of antisense RNA expression during cardiac MHC gene switching in response to pressure overload. *American Journal of Physiology-Heart and Circulatory Physiology* **2006**, *290* (6), H2351−H2361.
(31) Haddad, F.; Qin, A. Q. X.; Giger, J. M.; Guo, H. Y.; Baldwin, K. M. Potential pitfalls in the accuracy of analysis of natural sense-antisense RNA pairs by reverse transcription-PCR. *BMC Biotechnol.* **2007**, *7*, 21.
(32) Roberts, J. D.; Preston, B. D.; Johnston, L. A.; Soni, A.; Loeb, L. A.; Kunkel, T. A. Fidelity of two retroviral reverse transcriptases during DNA-dependent DNA synthesis in vitro. *Mol. Cell. Biol.* **1989**, *9* (2), 469−476.
(33) Varadaraj, K.; Skinner, D. M. Denaturants or Cosolvents Improve the Specificity of Pcr Amplification of a G+C-Rich DNA Using Genetically-Engineered DNA-Polymerases. *Gene* **1994**, *140* (1), 1−5.
(34) Ståhlberg, A.; Kubista, M.; Pfaffl, M. Comparison of reverse transcriptases in gene expression analysis. *Clin. Chem.* **2004**, *50* (9), 1678−1680.
(35) Kozarewa, I.; Ning, Z.; Quail, M. A.; Sanders, M. J.; Berriman, M.; Turner, D. J. Amplification-free Illumina sequencing-library preparation facilitates improved mapping and assembly of (G+C)-biased genomes. *Nat. Methods* **2009**, *6* (4), 291−295.
(36) Qian Wu, J.; Du, J.; Rozowsky, J.; Zhang, Z.; Urban, A. E.; Euskirchen, G.; Weissman, S.; Gerstein, M.; Snyder, M. Systematic analysis of transcribed loci in ENCODE regions using RACE sequencing reveals extensive transcription in the human genome. *Genome Biology* **2008**, *9* (1), R3.

https://dx.doi.org/10.1021/acsphotonics.0c01486
ACS Photonics 2021, 8, 424−430

(37) Langer, J.; Jimenez de Aberasturi, D.; Aizpurua, J.; Alvarez-Puebla, R. A.; Auguié, B.; Baumberg, J. J.; Bazan, G. C.; Bell, S. E.; Boisen, A.; Brolo, A. G.; et al. Present and future of surface-enhanced Raman scattering. *ACS Nano* **2020**, *14* (1), 28−117.
(38) Verma, P. Tip-enhanced Raman spectroscopy: technique and recent advances. *Chem. Rev.* **2017**, *117* (9), 6447−6466.
(39) Pozzi, E. A.; Goubert, G.; Chiang, N.; Jiang, N.; Chapman, C. T.; McAnally, M. O.; Henry, A.-I.; Seideman, T.; Schatz, G. C.; Hersam, M. C.; Duyne, R. P. V. Ultrahigh-vacuum tip-enhanced Raman spectroscopy. *Chem. Rev.* **2017**, *117* (7), 4961−4982.
(40) Deckert-Gaudig, T.; Taguchi, A.; Kawata, S.; Deckert, V. Tip-enhanced Raman spectroscopy-from early developments to recent advances. *Chem. Soc. Rev.* **2017**, *46* (13), 4077−4110.
(41) Wang, X.; Huang, S.-C.; Huang, T.-X.; Su, H.-S.; Zhong, J.-H.; Zeng, Z.-C.; Li, M.-H.; Ren, B. Tip-enhanced Raman spectroscopy for surfaces and interfaces. *Chem. Soc. Rev.* **2017**, *46* (13), 4020−4041.
(42) Bonhommeau, S.; Lecomte, S. Tip-enhanced Raman spectroscopy: A tool for nanoscale chemical and structural characterization of biomolecules. *ChemPhysChem* **2018**, *19* (1), 8−18.
(43) Olschewski, K.; Kämmer, E.; Stöckel, S.; Bocklitz, T.; Deckert-Gaudig, T.; Zell, R.; Cialla-May, D.; Weber, K.; Deckert, V.; Popp, J. A manual and an automatic TERS based virus discrimination. *Nanoscale* **2015**, *7* (10), 4545−4552.
(44) Neugebauer, U.; Rösch, P.; Schmitt, M.; Popp, J.; Julien, C.; Rasmussen, A.; Budich, C.; Deckert, V. On the way to nanometer-sized information of the bacterial surface by tip-enhanced Raman spectroscopy. *ChemPhysChem* **2006**, *7* (7), 1428−1430.
(45) Najjar, S.; Talaga, D.; Schué, L. o.; Coffinier, Y.; Szunerits, S.; Boukherroub, R.; Servant, L.; Rodriguez, V.; Bonhommeau, S. b. Tip-enhanced Raman spectroscopy of combed double-stranded DNA bundles. *J. Phys. Chem. C* **2014**, *118* (2), 1174−1181.
(46) Japaridze, A.; Vobornik, D.; Lipiec, E.; Cerreta, A.; Szczerbinski, J.; Zenobi, R.; Dietler, G. Toward an effective control of DNA's submolecular conformation on a surface. *Macromolecules* **2016**, *49* (2), 643−652.
(47) Lin, X.-M.; Deckert-Gaudig, T.; Singh, P.; Siegmann, M.; Kupfer, S.; Zhang, Z.; Gräfe, S.; Deckert, V. Direct base-to-base transitions in ssDNA revealed by tip-enhanced Raman scattering. *arXiv preprint arXiv:1604.06598* **2016**, na.
(48) He, Z.; Han, Z.; Kizer, M.; Linhardt, R. J.; Wang, X.; Sinyukov, A. M.; Wang, J.; Deckert, V.; Sokolov, A. V.; Hu, J.; Scully, M. O. Tip-enhanced raman imaging of single-stranded DNA with single base resolution. *J. Am. Chem. Soc.* **2019**, *141* (2), 753−757.
(49) Zhang, R.; Zhang, Y.; Dong, Z. C.; Jiang, S.; Zhang, C.; Chen, L. G.; Zhang, L.; Liao, Y.; Aizpurua, J.; Luo, Y.; Yang, J. L.; Hou, J. G. Chemical mapping of a single molecule by plasmon-enhanced Raman scattering. *Nature* **2013**, *498* (7452), 82−86.
(50) Chen, C.; Hayazawa, N.; Kawata, S. A 1.7 nm resolution chemical analysis of carbon nanotubes by tip-enhanced Raman imaging in the ambient. *Nat. Commun.* **2014**, *5* (1), 1−5.
(51) Liu, P.; Chulhai, D. V.; Jensen, L. Single-molecule imaging using atomistic near-field tip-enhanced Raman spectroscopy. *ACS Nano* **2017**, *11* (5), 5094−5102.
(52) Deckert-Gaudig, T.; Kurouski, D.; Hedegaard, M. A.; Singh, P.; Lednev, I. K.; Deckert, V. Spatially resolved spectroscopic differentiation of hydrophilic and hydrophobic domains on individual insulin amyloid fibrils. *Sci. Rep.* **2016**, *6*, 33575.
(53) Lee, J.; Crampton, K. T.; Tallarida, N.; Apkarian, V. A. Visualizing vibrational normal modes of a single molecule with atomically confined light. *Nature* **2019**, *568* (7750), 78−82.
(54) Madzharova, F.; Heiner, Z.; Gühlke, M.; Kneipp, J. Surface-enhanced hyper-Raman spectra of adenine, guanine, cytosine, thymine, and uracil. *J. Phys. Chem. C* **2016**, *120* (28), 15415−15423.
(55) Guo, L.; Wang, R.; Xu, H.; Liang, J. Why can the carbon nanotube tips increase resolution and quality of image in biological systems? *Phys. E* **2005**, *27* (1−2), 240−244.
(56) Kawai, T.; Tanaka, H.; Nakagawa, T. Low dimensional self-organization of DNA-base molecules on Cu (111) surfaces. *Surf. Sci.* **1997**, *386* (1−3), 124−136.
(57) Huang, X.; Gao, Y.; Yang, T.; Ren, W.; Cheng, H.-M.; Lai, T. Quantitative Analysis of Temperature Dependence of Raman shift of monolayer WS2. *Sci. Rep.* **2016**, *6*, 32236.
(58) Read, J. M.; Bridgen, J. R.; Cummings, D. A.; Ho, A.; Jewell, C. P. Novel coronavirus 2019-nCoV: early estimation of epidemiological parameters and epidemic predictions. *MedRxiv* **2020**, na.
(59) Li, Q.; Guan, X.; Wu, P.; Wang, X.; Zhou, L.; Tong, Y.; Ren, R.; Leung, K. S.; Lau, E. H.; Wong, J. Y.; et al. Early transmission dynamics in Wuhan, China, of novel coronavirus-infected pneumonia. *N. Engl. J. Med.* **2020**, *382* (13), 1199−1207.
(60) Wu, J. T.; Leung, K.; Leung, G. M. Nowcasting and forecasting the potential domestic and international spread of the 2019-nCoV outbreak originating in Wuhan, China: a modelling study. *Lancet* **2020**, *395* (10225), 689−697.

https://dx.doi.org/10.1021/acsphotonics.0c01486
ACS Photonics 2021, 8, 424−430